Available online at www.sciencedirect.com

ScienceDirect

Underground Space 7 (2022) 1139–1155

www.keaipublishing.com/undsp

Undrained stability of pit-in-pit braced excavations under hydraulic uplift

Fengwen Lai [a,b], Fuquan Chen [c], Songyu Liu [a,*], Suraparb Keawsawasvong [d], Jim Shiau [e]

[a] Institute of Geotechnical Engineering, Southeast University, Nanjing 211189, China
[b] Faculty of Civil Engineering and Geosciences, Delft University of Technology, PO-box 5048, 2628 CN Delft/2600 GA Delft, The Netherlands
[c] College of Civil Engineering, Fuzhou Univ, Fuzhou 350116, China
[d] Department of Civil Engineering, Thammasat School of Engineering, Thammasat Univ, Pathumthani 12120, Thailand
[e] School of Engineering, University of Southern Queensland, Toowoomba, QLD, 4350, Australia

Received 31 July 2021; received in revised form 15 February 2022; accepted 29 April 2022
Available online 20 July 2022

Abstract

Pit-in-pit (PIP) excavations in an aquifer–aquitard system likely undergo catastrophic failures under the hydraulic uplift, the associated undrained stability problem, however, has not been well analyzed in the past. To this end, a hypothetical model of PIP braced excavation in typical soil layers of Shanghai, China is developed using the finite element limit analysis (FELA) tool. The FELA solutions of safety factors (FSs) against hydraulic uplift are verified with the results from the finite element analysis with strength reduction technique (SRFEA) and existing design approaches. Subsequently, FELA is employed to identify the triggering and failure mechanisms of PIP braced excavations subjected to hydraulic uplift. A series of parametric studies considering the various geometric configurations of the PIP excavation, undrained shear strengths of aquitard, and artesian pressures are carried out. The sensitivities of relevant design parameters are further assessed using a multivariate adaptive regression splines (MARS) model that is capable of accurately capturing the nonlinear relationships between a set of input variables and output variables in multi-dimensions. A MARS-based design equation used for predicting FS is finally presented using the artificial dataset from FELA for practical design uses.

Keywords: Pit-in-pit excavation; Hydraulic uplift; Undrained stability; Finite element limit analysis; Multivariate adaptive regression splines

1 Introduction

The fast growth in urban populations leads to an increasing demand to maximize the utilization of underground space. The re-excavation activities at the base are, as a result, always required to meet the multi-functional needs of practical projects (e.g., elevator shafts, water-collecting wells, basements with various depths). This unique form of excavation, composed of the outer pit and the inner, is commonly known as the pit-in-pit (PIP) excavation (Sun et al., 2017, 2018; Tan et al., 2018; Wang et al., 2020; Chen et al., 2020; Sun & Xiao, 2021). Under this context, especially in some coastal dense urban areas, the complicated surrounding environments and geological conditions pose great challenges to geotechnical engineers (Lai et al., 2020b, 2021, 2022a).

The soil profiles in coastal areas are almost characterized by clayey stratum overlying sandy stratum, forming an aquitard–confined aquifer system. The underlying stability analyses (e.g., triggering and failure mechanisms) are extremely complicated under the coupled effects of hydraulic uplift and re-excavation. (Cashman & Preene, 2003; Zhou et al., 2010; Wu et al., 2016; Shi et al., 2018; Zhang et al., 2018). For PIP excavations involved in this system, catastrophic failures have been worldwide reported because of hydraulic uplift (Chow & Ou, 1999; Liu et al., 2011; Ng et al., 2012; Hong & Ng, 2013; Pujades et al.,

* Corresponding author.
E-mail address: liusy@seu.edu.cn (S. Liu).

https://doi.org/10.1016/j.undsp.2022.04.003

2014; Hong et al., 2015; Hong & Wang, 2016; Zhang et al., 2016).

Over past decades, research emphasis has been placed on the performances of deep excavations under hydraulic uplift using field observations, laboratory tests, and/or numerical modeling. For example, Milligan and Lo (1970) observed the field performance of eight excavations destabilized by hydraulic uplift and reported the large basal upheaval displacement and ground settlement behind supporting walls. Moore and Longworth (1979) carried out the field measurement to observe the construction process of deep excavations in Oxford clays above a confined aquifer. Shi et al. (2018) investigated the far-ground response of groundwater to pumping artesian water in deep excavations. Although field observations generally require alarge number of resources (material, equipment, and manpower), they are limited in reporting the triggering mechanisms of base instability of deep excavations.

On the other hand, laboratory test equipment such as calibration chambers and centrifuge devices can be relatively well-controlled, thus essentially facilitating more intensive observations. Hong and Ng (2013) performed two groups of centrifuge tests to model in-flight multi-propped excavations in soft clays above a confined aquifer with and without anti-uplift piles under hydraulic uplift. Also, a series of centrifuge tests were conducted by Sun (2016), and two typical failure modes due to hydraulic uplift were identified: the local failure and the general uplift failure. It was found that comparatively few experimental studies on deep excavations subjected to hydraulic uplift were reported in the past decade.

Numerical modeling, primarily finite element method and discrete element method, is a powerful and cost-effective tool, which can more accurately consider the stress history and stress–strain relationship due to excavation activities. Seepage resulted from dewatering during excavation can also be involved to numerically assess the overall stability of PIP excavation problems. Hong et al. (2015) conducted the back analyses by finite element (FE) method and stated that the triggering and failure mechanisms of base instability of the general excavation were mainly governed by a ratio of excavation width to thickness of soft clay inside the excavation. Ding et al. (2014) numerically reported that the thickness of the confined aquifer inside the excavation plays an important role in resisting the hydraulic uplift. Recently, Zhang et al. (2018) developed a hypothetical excavation model with multi-aquitard-aquifer systems in Shanghai, which was further incorporated in finite difference software to examine the effect of dewatering in a confined aquifer on the surface ground movements. Recently, a relatively novel numerical technique, known as the finite element limit analysis (FELA) (Sloan, 2013), was developed and implemented in OptumG2 code, which is capable of handling extremely complex boundaries with high efficiency. Chen et al. (2020) recently employed the FELA to investigate the base instability triggered by the hydraulic uplift of PIP braced excavations. The advantages of using the FELA in modeling the hydraulic uplift for the underground excavation problem were discussed in their work.

Although the performance of base excavation subjected to hydraulic uplift has been broadly discussed in previously-published works, the interpretation into triggering and failure mechanisms of PIP excavations, as well as the effects of re-excavation (transition zone between inner and outer pits), is nevertheless not available. Both wall displacement and ground deformation of PIP excavations in soft soils were studied by several researchers (Sun et al., 2017; Sun et al., 2018; Tan et al., 2018; Wang et al., 2020; Sun & Xiao, 2021), but the influence of hydraulic uplift was not taken into consideration. Moreover, little attention was paid to the undrained stability of PIP excavations comprehensively considering re-excavation and hydraulic uplift.

Currently, the traditional theoretical approach to assess the undrained stability of PIP excavations is the "pressure balance method" presented by Terzaghi (1943). The results obtained are often assumed to be overly conservative because only the effect of soil deadweight is involved. An extension of Terzaghi's method is due to Wudtke (2008), who further considered the effect of the undrained shear strength of aquitard. Additionally, Yang and Zheng (2009) deduced an analytical solution for FS against hydraulic uplift by quantitatively considering the effect of slip surfaces of excavations. The existing approaches for assessing the undrained stability of PIP excavations subjected to hydraulic uplift, however, are rather limited due to the neglect of re-excavation. It is, therefore, expected to present a new design method used for undrained stability analyses, with overall consideration of the shear strength of aquitard, re-excavation (transition zone), artesian pressure, and failure mechanisms involved.

This paper aims at providing new insights into the triggering and failure mechanisms of a PIP braced excavation with an aquifer-aquitard system. A hypothetical model of PIP braced excavation involving typical soil layers is developed in FELA software, accounting for the coupling effects between re-excavation and variations of artesian pressure. A comparison of the factors of safety (FSs) calculated by existing theoretical methods and the FE model is carried out to demonstrate the accuracy of the developed FELA model. Thereafter, the undrained stability assessment is conducted, and a new design equation based on a multivariate adaptive regression splines (MARS) model is proposed to estimate the FS against hydraulic uplift.

2 Problem definition

To assess the undrained stability and explore the triggering and failure mechanisms of PIP excavations subjected to hydraulic uplift, a typical multi-strutted PIP excavation with a narrow-long shape in Shanghai, China is shown in Fig. 1.

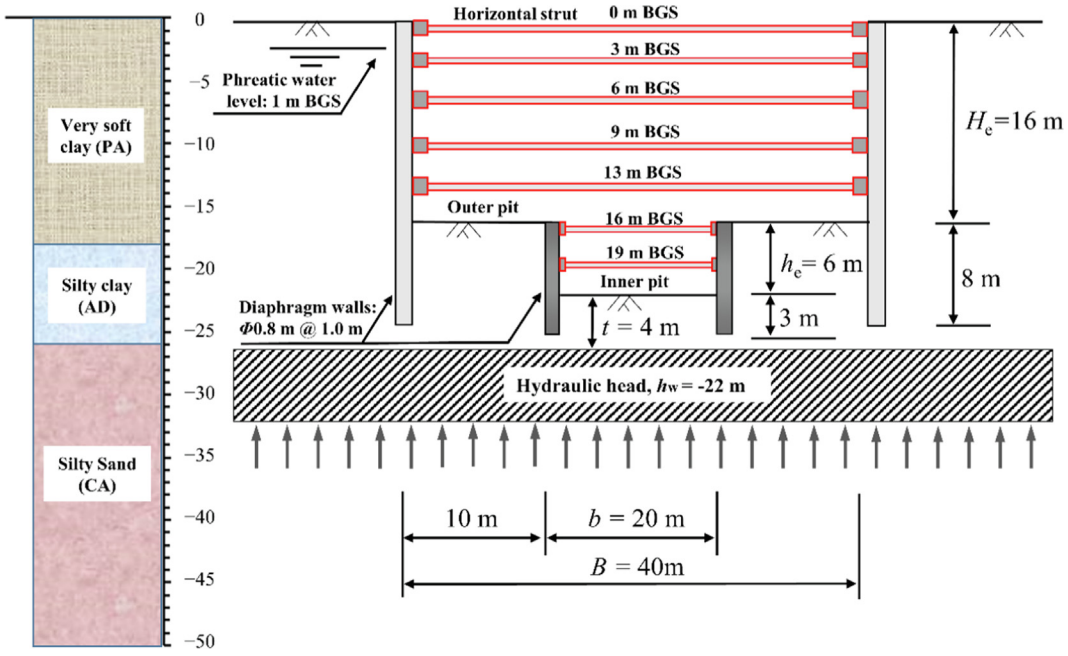

Fig. 1. A typical PIP braced excavation in soft clays overlying a confined aquifer.

Shanghai soil was deposited in the Yangtze River Delta in the Late Pleistocene and Holocene eras. The general engineering properties of Shanghai strata have been extensively reported by many researchers (Wu et al., 2015; Ye & Ye, 2016; Ye et al., 2018; Tiwari et al., 2020). For simplification, the representative soil layers are ④, ⑥, and ⑦ (i.e., very soft clay L4, silty clay L6, and silty sand L7). The base of PIP braced excavation is close to the soil layer L7 with high permeability and high artesian pressure, i.e., a confined aquifer (CA). CA is 24 m in thickness, greatly compromising the base stability of PIP braced excavation. The soft clayey strata overlying CA are a phreatic aquifer (PA) with a thickness of 18 m and an aquitard (AD) with a thickness of 8 m, respectively.

A typical PIP braced excavation problem is shown in Fig. 1 under the plane strain condition. The long-term groundwater level (phreatic water level) was 1 m below ground surface (BGS). A PIP braced excavation contained an inner pit (6 m in depth h_e and 20 m in width b) and an outer pit (16 m in depth H_e and 40 m in width B). Therefore, the width of the platform between the inner pit and the outer was 10 m, the thickness of AD inside the inner pit was 4 m. Both the inner and outer pits were supported by multiple horizontal struts and diaphragm walls. The embedded depth of outer walls was 8 m, and that of inner ones was 3 m. The PIP system was subdivided into seven excavating layers, and excavated in steps. The excavation depth of each layer was 3 m BGS, 6 m BGS, 10 m BGS, 13 m BGS, 16 m BGS (base of the outer pit), 19 m BGS, and 22 m BGS (base of the inner pit), respectively. Dewatering before excavation was required at each stage. The phreatic water level was lowered to 1 m below the base in each excavation stage. Five levels of horizontal struts in the outer pit were installed after completion of each layer at 0 m BGS, 3 m BGS, 6 m BGS, 10 m BGS, and 13 m BGS, respectively. Similarly, there also existed two levels of horizontal struts in the inner pit and installed respectively at 16 m BGS and 19 m BGS.

The height of the initial hydraulic head of the confined aquifer was assumed to be 10 m BGS, resulting in the action of hydraulic pressure of $h_w = -22$ m at 30 m BGS, as shown in Fig. 1. The dewatering wells were set to reduce the artesian pressure of the confined aquifer before excavation. After the outer pit was fully dewatered and excavated, the hydraulic head of the underground water was reduced to 22 m BGS. The sequence of construction stages is summarized in Table 1. Stage 1 to Stage 18 were performed by employing the elastoplastic finite element analysis (FEA) to generate the stress and hydraulic head fields induced from the construction sequence. The upper bound (UB) and lower bound (LB) FELA were carried out at the final stage to determine more realistic failure modes and FSs against hydraulic uplift. More details regarding the FELA are described later.

3 FELA model details

3.1 Use of FELA

FELA is a numerical technique based on a limit analysis framework involving plasticity theorem, finite element discretization, and mathematical programming. That is, under the framework of the plastic bound theorem, FELA subtly uses the FE discretization for addressing the complicated soil stratifications and loadings as well as boundary

Table 1
Main construction stages and modeling activities in FELA.

Stage	Modeling activity	Computing method
1	Initial stress computation	Computation by K_0 analysis
2	Installation of outer diaphragm wall	Elasto-plastic analysis
3	Dewatering PA to BGS 4.0 m (level 1), and excavating to BGS 3.0 m	Elasto-plastic analysis
4	Casting of horizontal strut 1 at BGS 0 m	Elasto-plastic analysis
5	Dewatering PA to BGS 7.0 m (level 2), and excavating to BGS 6.0 m	Elasto-plastic analysis
6	Casting of horizontal strut 2 at BGS 3.0 m	Elasto-plastic analysis
7	Dewatering PA to BGS 11.0 m (level 3), and excavating to BGS 10.0 m	Elasto-plastic analysis
8	Casting of horizontal strut 3 at BGS 6.0 m	Elasto-plastic analysis
9	Dewatering PA to BGS 14.0 m (level 4), and excavating to BGS 13.0 m	Elasto-plastic analysis
10	Casting of horizontal strut 4 at BGS 9.0 m	Elasto-plastic analysis
11	Dewatering PA to BGS 17.0 m (level 5), and excavating to BGS 16.0 m	Elasto-plastic analysis
12	Casting of horizontal strut 5 at BGS 13.0 m	Elasto-plastic analysis
13	Setting hydraulic head h_w of AqⅡ to a specific value	Elasto-plastic analysis
14	Installation of inner diaphragm wall	Elasto-plastic analysis
15	Dewatering AD to BGS 21.0 m (level 6), and excavating to BGS 20.0 m	Elasto-plastic analysis
16	Casting of horizontal strut 6 at BGS 16.0 m	Elasto-plastic analysis
17	Dewatering AD to BGS 24.0 m (level 7), and excavating to BGS 23.0 m	Elasto-plastic analysis
18	Casting of horizontal strut 7 at BGS 19.0 m	Elasto-plastic analysis
19	Determination of failure mode and FS against hydraulic uplift	FELA (UB/LB)

conditions to bracket the rigorous UB and LB solutions of the exact ultimate loads or FSs. FELA has been widely used to study a variety of complex stability problems as the computational efficiency is improved significantly (Chen, 1975; Sloan & Kleeman, 1995; Sloan, 2013). FELA postulates that the rigid-perfectly plastic material obeys the associated flow rule. More details of FELA are omitted here and can be found in Sloan (2013).

In this study, the adaptive FELA with second-order cone programming (SOCP) software, OptumG2 (Krabbenhoft et al., 2015), was used to accurately determine the rigorous UB and LB FSs, and to interpret the failure mechanisms of PIP braced excavations under hydraulic uplift. For the UB analysis in OptumG2, the solid elements for soil masses are six-node triangular elements. At each node of the UB triangular elements, the unknown velocity components use a quadratic interpolation within each element and are continuous between adjacent elements. For the LB analysis in OptumG2, the solid elements for soil masses are three-noded triangular elements. Each element of the LB triangular elements has their unique node. These nodes allow possible stress discontinuities to take place along shared edges of adjacent elements. The LB and UB calculations are formulated as SOCP to obtain the FSs of PIP braced excavations. Till now, OptumG2 has been successfully employed to solve various undrained stability problems, including excavations (Keawsawasvong & Ukritchon, 2017a, Keawsawasvong & Ukritchon, 2019; Chen et al., 2020), slopes (Yang et al., 2016; Oberhollenzer et al., 2018), pile foundations (Keawsawasvong & Ukritchon, 2017b; Zhou et al., 2020b), marine infrastructures (Ke et al., 2020), earth retaining structures (Lai et al., 2022b; Yang et al., 2022), and trapdoor problems (Keawsawasvong & Ukritchon, 2017c; Lai et al., 2020a; Shiau et al., 2021, 2022).

3.2 HMC constitutive model

In the FELA model, the soils were simulated by Hardening Mohr–Coulomb (HMC) constitutive model considering soil-hardening behaviours under loading or unloading. HMC model was first proposed for three-dimensional spatial stress surfaces by Wood (2004), and further extended to the general stress space by Doherty and Muir Wood (2013). HMC model remains some advantages of Mohr–Coulomb (MC) constitutive model, such as the simplicity in modeling, and the fewer and easy access to the model parameters. Also, it overcomes some shortcomings of the MC model, e.g., the inability to accurately analyze the deformation behaviors of the soils. Therefore, the HMC model can be applied to perform the stability analysis considering the different stress paths of soils in PIP excavations. HMC model characterizes the variety of soil stiffness caused by the change of soil stress level using stiffness parameters (i.e., E_{50}, E_{ur}, and ν_{ur}). The typical behavior of soils in drained triaxial compression experiments is shown in Fig. 2. E_{50} represents the secant Young's modulus, and can be defined as

$$E_{50} = \frac{q_u}{2\varepsilon_{1,50}}, \tag{1}$$

where the ultimate shear stress of $q_u = (\sigma_1 - \sigma_3)_u$, and $\varepsilon_{1,50}$ is the axial strain corresponding to the half ultimate shear stress. Similarly, the stiffness is represented by Young's modulus E_{ur} and Poisson's ratio ν_{ur} in unloading/reloading. Both E_{ur} and ν_{ur} are the elastic parameters, while E_{50} is composed of elastic and plastic characteristics. Generally, both the values of E_{50} and E_{ur} are dependent on the soil pressure and increase with increasing confining pressure. This also indicates that the soil stiffness is related to the stress level, as shown in Eqs. (2) and (3):

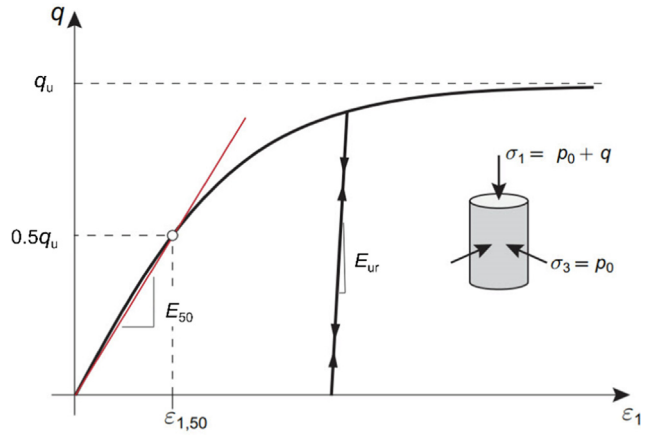

Fig. 2. Typical behavior of soil mass in drained triaxial compression (adapted from Krabbenhoft et al. (2015)).

$$E_{50} = E_{50}^{\mathrm{ref}} \left(\frac{c\cos\phi - \sigma'_3 \sin\phi}{c\cos\phi + p^{\mathrm{ref}} \sin\phi} \right)^m, \tag{2}$$

$$E_{\mathrm{ur}} = E_{\mathrm{ur}}^{\mathrm{ref}} \left(\frac{c\cos\phi - \sigma'_3 \sin\phi}{c\cos\phi + p^{\mathrm{ref}} \sin\phi} \right)^m, \tag{3}$$

where E_{50}^{ref} is the secant Young's modulus in triaxial drained compression under confining pressure p^{ref}, $E_{\mathrm{ur}}^{\mathrm{ref}}$ is the Young's modulus in unloading/reloading at a reference pressure p^{ref}, σ'_3 is the confining pressure in triaxial test, c is the soil cohesion and ϕ is the soil friction angle, and m is the power exponent related to stress level and depends on the soil type. It was assumed that $m = 0.5$ for granular materials, while $m = 1.0$ for very soft soils (Wood, 2004).

3.3 Numerical model

Following the problem definition in Fig. 1, the numerical model was established as shown in Fig. 3. The dimensions of 100 m in the x-direction and 50 m in the y-direction were fixed to avoid the possible error resulting from the boundary effects on the performance of PIP excavations. The clayey and sandy soils were both simulated by the HMC model with the non-associated flow rule at stages of ealsto-plastic analyses. However, it should be noted that since the FELA explicitly postulates the associated plasticity, all soil layers have to be defaulted with associated flow rule at the last modelling step to obtain a clear indication of the failure mode (Table 1). The soils were modeled as 15-node triangular solid elements with 12 Gauss integration stress points, which was well-accepted for deformation analysis. The enclosed diaphragm walls were represented by the plate elements, and the fixed end anchors were used to simulate the horizontal struts. The vertical boundaries of the symmetrical model were horizontally constrained ($\Delta x = 0$, $\Delta y \neq 0$). Full fixities ($\Delta x = 0$, $\Delta y = 0$) were ascribed at the bottom boundary, whilst the top was free ($\Delta x \neq 0$, $\Delta y \neq 0$)..

The non-seepage boundaries are similar to the impervious barriers at the left (i.e., C. L.) and the bottom boundaries (i.e., the confined aquifer overlying aquitard). The vertical fixed hydraulic head was set as 1 m BGS in the PA to simulate the constant phreatic water level of the model boundary. The groundwater level was gradually lowered to 1 m below the excavation base to simulate the dewatering of PIP excavations in steps. A horizontal fixed hydraulic head of 10 m BGS was imposed at the top of the CA to generate the artesian pressure. After the outer pit was fully dewatered and excavated, the hydraulic head of the groundwater was further reduced to 22 m BGS for the safe. To analyze the undrained stability, the fixed hydraulic head was gradually increased to 20 m BGS, 18 m BGS, 16 m BGS, 14 m BGS, etc. until the instability occurred in PIP excavations.

The interface elements were used to model the interactions between the diaphragm walls and surrounding soils. The elastic and plastic deformations because of the relative displacements of wall-soil interfaces were calculated by the Mohr–Coulomb yield criterion, considering the elasto-plastic characteristics of the interface elements. The strength parameters of the interfaces were obtained by the product of the strength reduction factor R_{inter} and shear strength parameters of surrounding soils, as below:

$$c_{\mathrm{i}} = R_{\mathrm{inter}} c_{\mathrm{soil}}, \tag{4}$$

$$\tan\phi_{\mathrm{i}} = R_{\mathrm{inter}} \tan\phi_{\mathrm{soil}}. \tag{5}$$

Mesh Fan feature, working as a tool in Optum G2, was applied to the toes of diaphragm walls to construct a fan of elements around the singularity in the numerical model, which resulted in the improved solutions. This Mesh Fan feature efficiently avoided the non-convergence of numerical solutions because of stress concentration, hence also strengthening the computational stability. In addition, the mesh adaptivity with 5 iterations was adopted to obtain the more accurate failure modes and numerical solutions. By employing the mesh adaptivity technique, more elements were added to the sensitive regions containing large shear strain gradients during the computation. In process of numerical calculation, an initial mesh with the number of 5000 elements was automatically set and increased to a final mesh with the number of 20 000 elements.

3.4 Input parameters

The model parameters of soil layers involved are summarized in Table 2. Additionally, a set of specific parameters (i.e., normal stiffness of $EA = 2.40 \times 10^7$ kN/m, the bending stiffness of $EI = 1.28 \times 10^6$ kN·m^2/m, and the thickness of 0.8 m) were defined for the diaphragm walls (Peng et al., 2022). Seven horizontal struts with compression stiffness of $EA = 1.68 \times 10^7$ kN and horizontal spacing distance of 5 m were installed in the PIP excavation (Chen et al., 2020).

The FS against hydraulic uplift can be expressed as a function:

$$\mathrm{FS} = f(S_{\mathrm{u}},\ \gamma,\ t,\ P,\ H_{\mathrm{e}}, B,\ h_{\mathrm{e}},\ b), \tag{6}$$

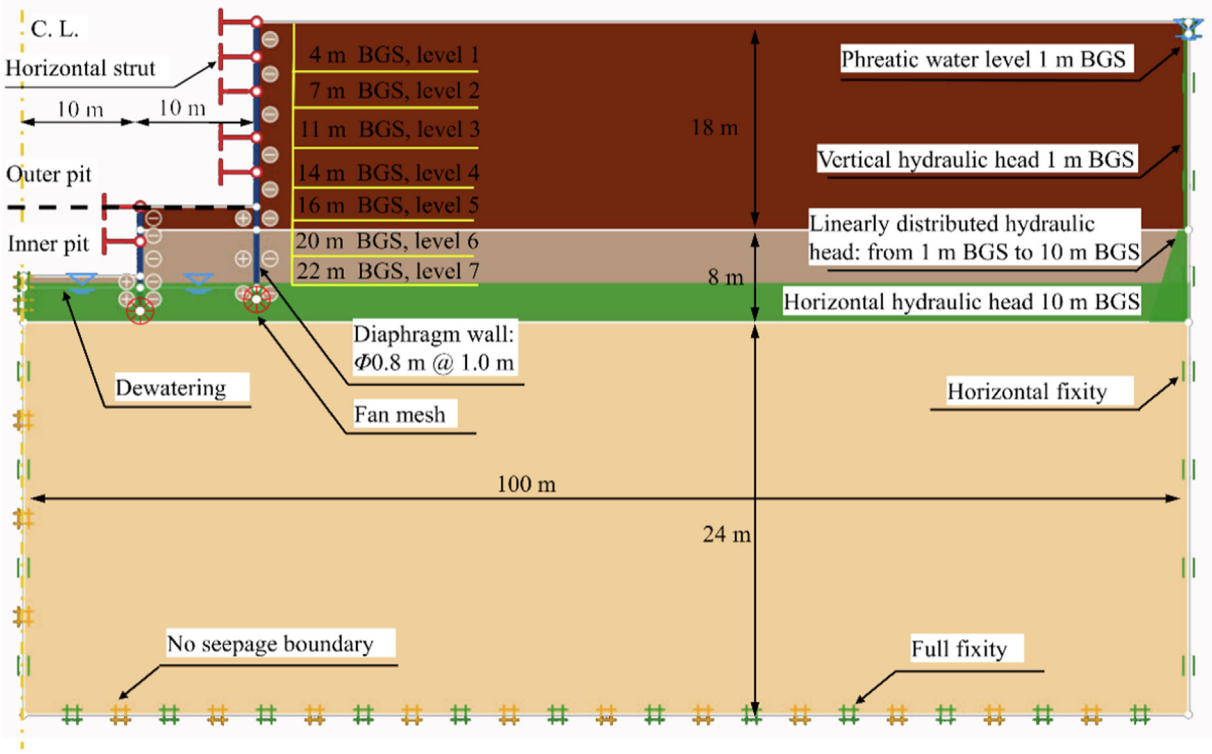

Fig. 3. Numerical model of a PIP braced excavation subjected to hydraulic uplift in OptumG2.

Table 2
Soil parameters used in FELA (Peng et al., 2022).

Definition	Symbol	Unit	L4	L6	L7
Thickness of soil layer	–	m	18.0	8.0	24.0
Unit weight	γ	kN·m^3	16.7	20	19
Undrained shear strength	S_u	kPa	35	80	NA
Effective cohesion	c'	kPa	NA[a]	NA	0.5
Effective internal friction angle	$\phi\prime$	°	NA	NA	32
Dilation angle	ψ	°	0	0	2[b]
Poisson's ratio in unloading/reloading at reference pressure[d]	v_{ur}	–	0.2	0.2	0.2
Secant Young's modulus in triaxial compression under confining pressure	E_{50}^{ref}	MPa	2.64	7.50	24.0
Young's modulus in unloading/reloading at reference pressure	E_{ur}^{ref}	MPa	15.40	22.50	48.0
Power exponent related stress level	m	–	0.8	0.8	0.5
Reference pressure[d]	p^{ref}	kPa	100	100	100
Interfacial strength reduction factor	R_{inter}	–	0.67[c]	0.67[c]	0.67[c]
Failure ratio	R_f	–	0.6	0.9	0.9
Coefficient of earth pressure under normal consolidation	K_0^{nc}	–	0.658	0.577	0.478
Permeability coefficient	k	cm/s	4.98×10^{-7}	4.63×10^{-8}	1.94×10^{-4}

[a] NA = not applicable
[b] Deduced from Bolton (1986) ($\psi' = \phi' - 30$)
[c] Recommended byBrinkgreve et al. (2002)
[d] Default value

where S_u and γ are the undrained shear strength and saturated unit weight of AD, respectively; t is the thickness of AD, and P is the artesian pressure acting upon the base of AD. The normalization method was used in the course of parametric study in terms of non-dimensional groups to include the effects of the dead weight of soils and the thickness of AD. Thus, Eq. (6) can be reduced to

$$FS = f[S_u/(\gamma t), P/(\gamma t), h_e/H_e, b/B], \quad (7)$$

where $S_u/(\gamma t)$ is the normalized undrained strength of AD, $P/(\gamma t)$ is the normalized artesian pressure on the base of AD, h_e/H_e is defined as the ratio of inner pit depth to outer pit depth, and b/B is defined as the ratio of inner pit width to outer pit width. Equation (7) suggests that the base instability of PIP excavation subjected to hydraulic uplift is mainly affected by four dimensionless groups (i.e., $S_u/(\gamma t)$, $P/(\gamma t)$, h_e/H_e, and b/B).

3.5 Comparison and validation

To validate the accuracy of the FELA method, a brief comparison was made against FS from FEA and existing design methods, as shown in Fig. 4. To the best of the author's knowledge, there is none of the available theoretical methods concerning the PIP concept to estimate the FS against hydraulic uplift. The calculation width of PIP braced excavation is thus assumed to be that of the outer pit, and the depth was considered to be the sum between inner pit depth and out pit depth. That is, the contribution of the transition zone to the stability of PIP excavations is neglected here. Terzaghi et al. (1968) only considered the contribution of the dead weight of the local zone of CA (so-called "Terzaghi-body") to resisting hydraulic uplift. Wudtke (2008) further accounted for the undrained shear strength of the Terzaghi-body. Yang and Zheng (2009) presented the homogeneous continuum method that CA inside the excavation can be deemed as a failure body, where the shear strength and deadweight can provide larger resistance. They are all the methods for usual foundation pits. To address this issue, a FE model was set up as a benchmark using PLAXIS 2D (Brinkgreve et al., 2002) with the Strength Reduction technique (SRFEA) (Tschuchnigg et al., 2015). The details of the FE model, in which the Hardening Soil (HS) model was used to simulate the base case, are fully consistent with the FELA model.

It is seen from Fig. 4 that the numerical results obtained from UB- and LB-FELA are in good agreement with those from SRFEA, giving confidence that FELA can accurately predict the solutions of FS against hydraulic uplift. In addition, the change laws of FS with $P/(\gamma t)$ obtained by using UB- and LB-FELA are consistent with those from existing design methods. However, the above design methods do not consider the effect of re-excavation and neglect the contribution of the transition zone to the undrained stability.

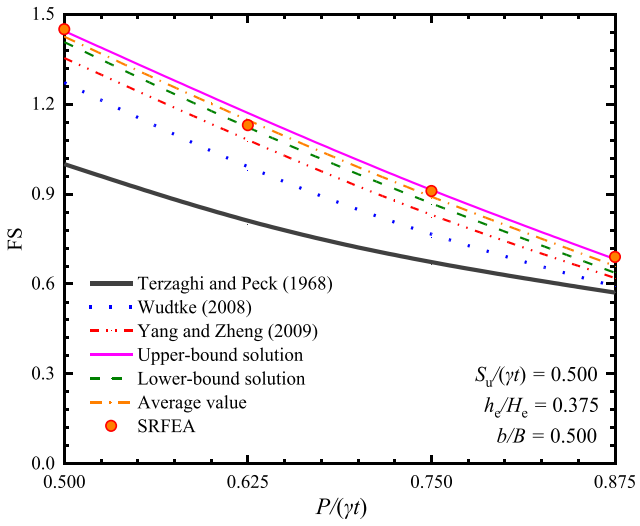

Fig. 4. Comparison of FSs obtained using FELA, SRFEA and existing design methods.

Therefore, it can be concluded that the theoretical solutions given by the existing design methods are lower than UB and LB solutions as well as their average values (UB + LB)/2. This finding demonstrates that the FELA method can provide a more reasonable and accurate stability assessment against hydraulic uplift of PIP excavations.

4 Triggering and failure mechanisms

4.1 Failure mechanisms

Figure 5(a)–(d) respectively present the shear dissipation contours, adaptive meshes, incremental displacement vectors, and groundwater flow vectors diagrams of the PIP braced excavation with $P/(\gamma t) = 0.250$, $S_u/(\gamma t) = 0.750$, $h_e/H_e = 0.375$ and $b/B = 0.500$. In this scenario, the artesian pressure on AD can be resisted by the down-thrust of the inner pit with the higher shear strength. The instability of the outer pit is mainly caused by the unloading effect, thus forming one circular slip surface for the outer pit, abbreviated as M1. The UB and LB solutions of FSs are 1.834 and 1.816, respectively. It can be also observed from the displacement vector diagrams in Fig. 5(c) that the phenomenon of soil uplift due to unloading at the base of the outer pit is prominent. Meanwhile, the groundwater flow mainly shows the seepage effect due to the dewatering at the excavation base. Greater stability may be expected for the inner pit in this scenario of PIP excavation, as the wider platform between the inner and outer pit can provide higher shearing resistance.

As the normalized undrained shear strength $S_u/(\gamma t)$ of AD is decreased to 0.500, Fig. 6(a) shows that the stability of the PIP braced excavation is weakened, and the circular plastic shear band would extend to the base of the inner pit. The corresponding failure mode can be defined as one circular slip surface for the PIP system (M2). In addition, a local plastic zone is found in the platform between the inner and outer pits. Therefore, the obvious displacement vectors can be also observed at both the bases of the inner and outer pits under the combined actions of unloading, seepage and hydraulic uplift (see Fig. 6(c)). The UB and LB solutions of FS are 1.252 and 1.237 for M2, respectively. The comparison of M1 and M2 shows that the local hydraulic uplift appears in the inner pit due to the lower shear strength of AD, thus causing the failure of the inner pit, as shown in Fig. 6(d).

Figure 7(a)–(d) respectively show the distribution of shear dissipation contours, adaptive meshes, incremental displacement vectors, and groundwater flow vectors diagrams of the PIP braced excavation with $P/(\gamma t) = 0.625$, $S_u/(\gamma t) = 0.500$, $h_e/H_e = 0.375$ and $b/B = 0.500$. In this scenario, the hydraulic uplift exceeds the soil resistance, i.e., deadweight and shear force, resulting in the wedge-cracking appearing in the base soils between the inner diaphragm wall and the C. L. of PIP braced excavation. The quasi-rigid wedges are then formed at the base of the inner pit similar to the "clay beam" discussed in Hong et al.

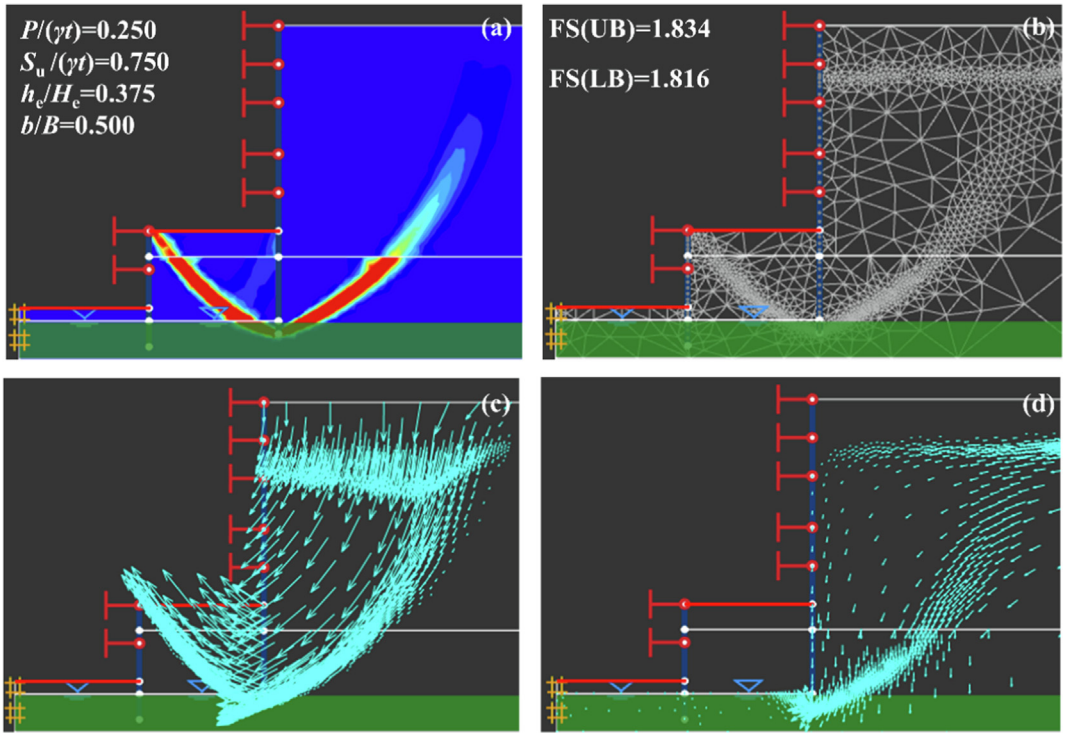

Fig. 5. Failure mode M1 of PIP braced excavation subjected to hydraulic uplift with $P/(\gamma t) = 0.250$, $S_u/(\gamma t) = 0.750$, $h_e/H_e = 0.375$ and $b/B = 0.500$: (a) shear dissipation contours, (b) adaptive meshes, (c) incremental displacement vectors, and (d) groundwater flow vectors.

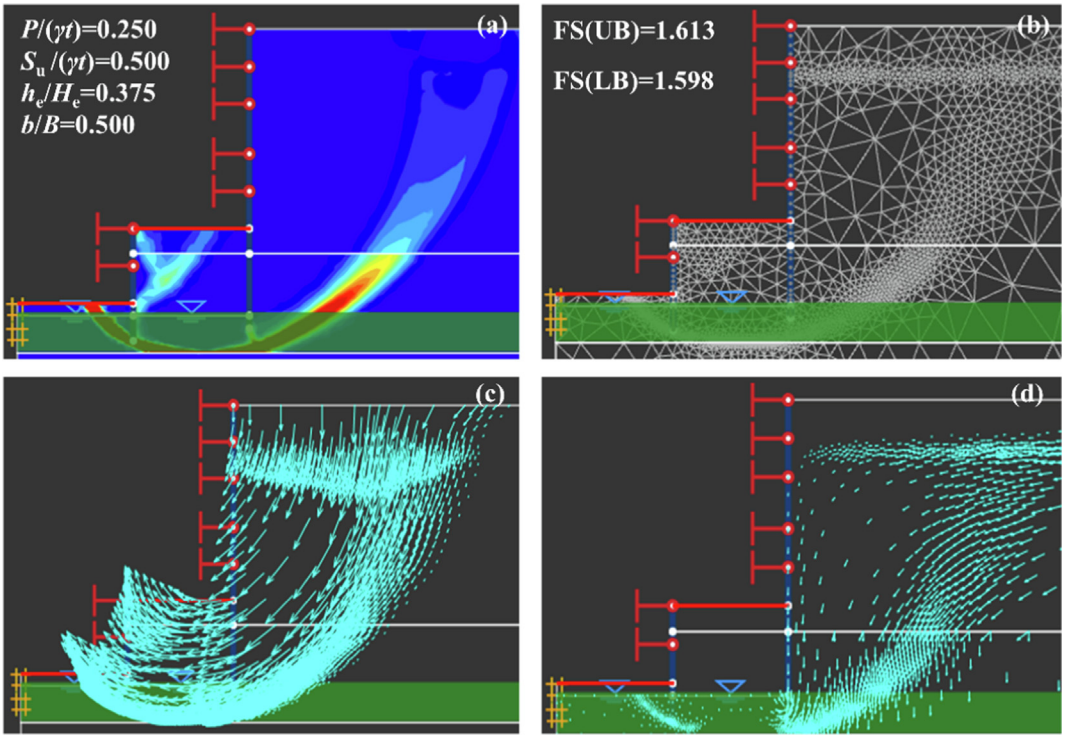

Fig. 6. Failure mode M2 of PIP braced excavation subjected to hydraulic uplift with $P/(\gamma t) = 0.250$, $S_u/(\gamma t) = 0.500$, $h_e/H_e = 0.375$ and $b/B = 0.500$: (a) shear dissipation contours, (b) adaptive meshes, (c) incremental displacement vectors, and (d) groundwater flow vectors.

(2015). At this critical stage, the whole PIP braced excavation is unstable due to the unloading and seepage effects. The combined failure mode can be described as a circular slip surface with a quasi-rigid wedge for the entire PIP system (see Fig. 7(a)). This is denoted as M3. The UB and LB solutions of FSs are 1.157 and 1.138, respectively. It can

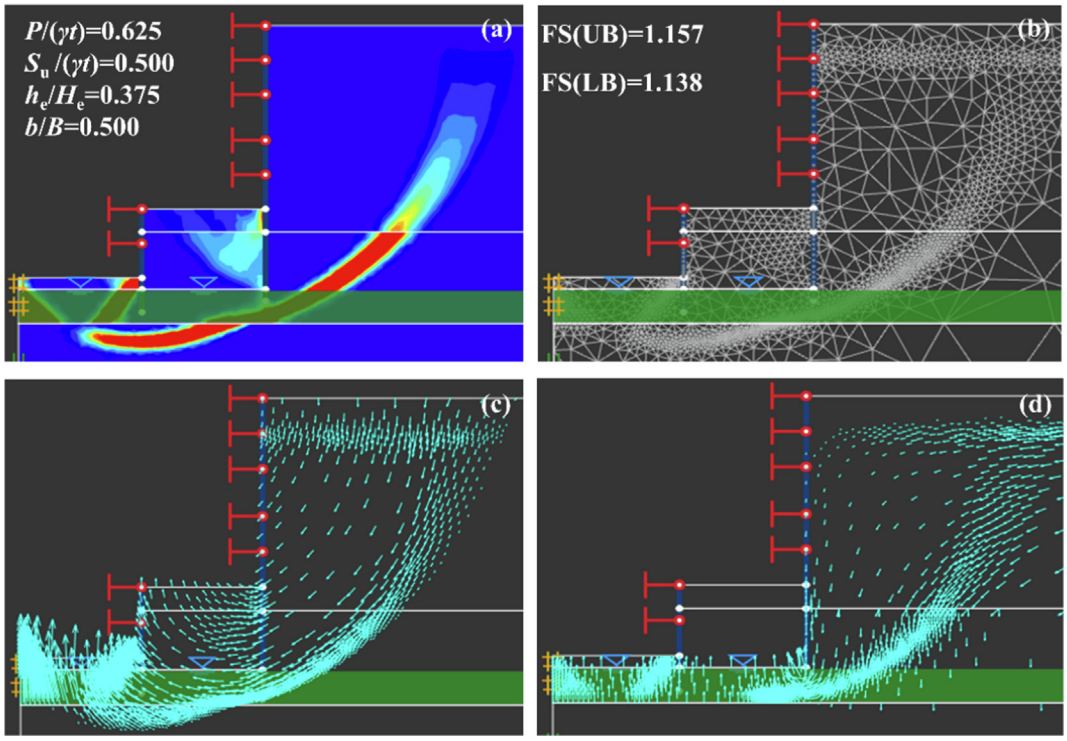

Fig. 7. Failure mode M3 of PIP braced excavation subjected to hydraulic uplift with $P/(\gamma t) = 0.625$, $S_u/(\gamma t) = 0.500$, $h_e/H_e = 0.375$ and $b/B = 0.500$: (a) shear dissipation contours, (b) adaptive meshes, and (c) incremental displacement vectors, and (d) groundwater flow vectors.

also be found from Fig. 7(c) that the upheaval deformation of base soils increases gradually from the inner or outer diaphragm wall to the C. L. with the maximum vertical displacement.

Based on the above scenario in Fig. 7, when increasing the normalized width of the inner pit to 0.800 (i.e., reducing the spacing between the inner and outer pits), the soils in the platform between the inner and outer pits (transition zone) would yield under the seepage force, forming a slip surface along the outer walls, as shown in Fig. 8. This phenomenon is similar to the hydraulic heave of a two-layered soil system with a relatively impervious top layer due to seepage forces. It is worth noting that the failure body in the platform due to the seepage effect is arc-shaped, rather than rectangular, triangular, and parabolic (Wudtke & Witt, 2006). In this scenario, under the comprehensive actions of seepage, hydraulic uplift, and unloading effect, a combined failure mode of one circular slip surface with basal hydraulic uplift for PIP system is formed, and this is defined as M4. The UB and LB solutions of the FS of the PIP braced excavation in this scenario are 1.075 and 0.993, respectively.

Figure 9(a)–(d) respectively show shear dissipation contours, adaptive meshes, incremental displacement vectors, and groundwater flow vectors diagrams of the PIP braced excavation with $P/(\gamma t) = 0.750$, $S_u/(\gamma t) = 0.500$, $h_e/H_e = 0.375$ and $b/B = 0.500$. The associated UB and LB solutions of FSs are 1.082 and 0.994, respectively. It is noted that the buoyancy uplift acting on the base of the AD in terms of surface forces, the shear force and dead-weight of the AD layer is unable to resist the artesian pressure with an increase in hydraulic head. This causes the hydraulic fracturing and basal hydraulic uplift for the inner pit, which is referred to as M5. In addition, there is no overall instability for the PIP braced excavation occurred in M5, but the base instability is triggered by hydraulic uplift for the inner pit. This phenomenon is due to the higher artesian pressure and the smaller thickness between the base of the inner pit and the top of CA. The distribution of the displacement vectors of the inner pit in M5 (see Fig. 9(c)) is similar to that in M3 and M4, as shown in Figs. 7(c) and 8(c).

In summary, it can be concluded that, regardless of the shapes of the slip surface, three distinct failure modes can be observed under the different combinations of normalized artesian pressure, normalized geometric configuration, and normalized undrained shear strength of AD: the circular slip surface, the basal hydraulic uplift, and the combined failure.

4.2 Triggering mechanisms

To further explore the triggering mechanisms due to basal hydraulic uplift in the failure mode M3, the distributions of principal stress and horizontal strain at the excavation base of the inner pit are shown in Fig. 10. It can be seen that the base soils are accompanied by horizontal displacements besides vertical upheaval displacements. The base soils in the inner pit are mainly subjected to horizontal compression stress σ_3 (negative value) in Zone 1, tending to

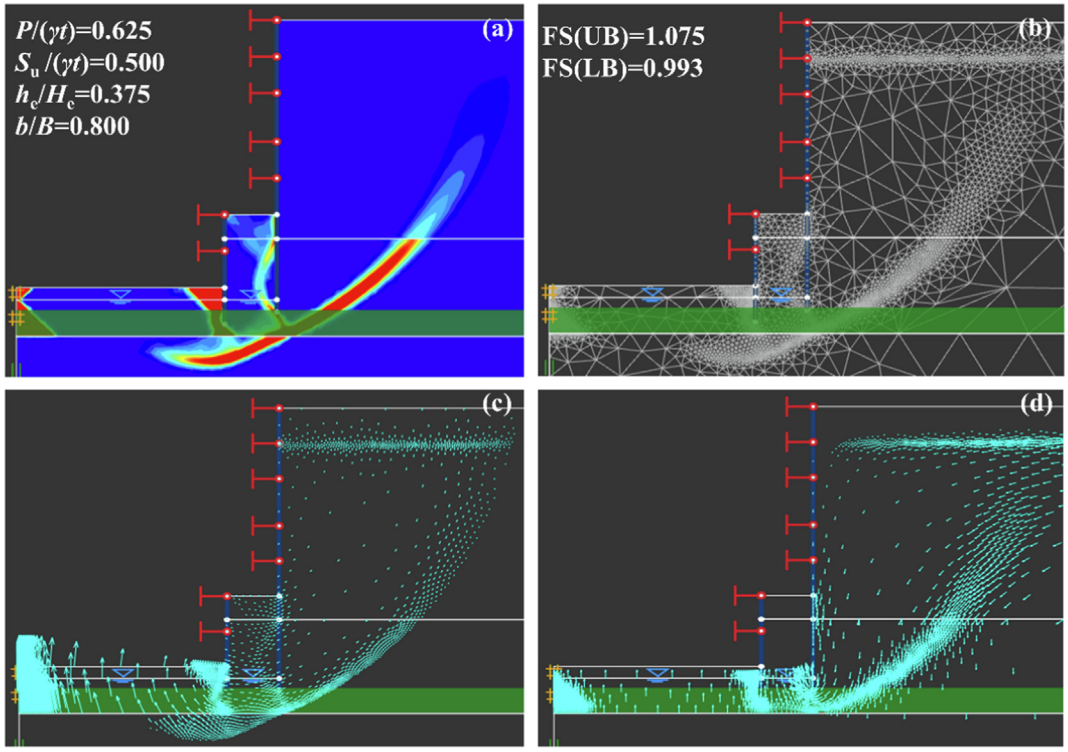

Fig. 8. Failure mode M4 of PIP braced excavation subjected to hydraulic uplift with $P/(\gamma t) = 0.625$, $S_u/(\gamma t) = 0.500$, $h_c/H_e = 0.375$ and $b/B = 0.800$: (a) shear dissipation contours, (b) adaptive meshes, (c) incremental displacement vectors, and (d) groundwater flow vectors.

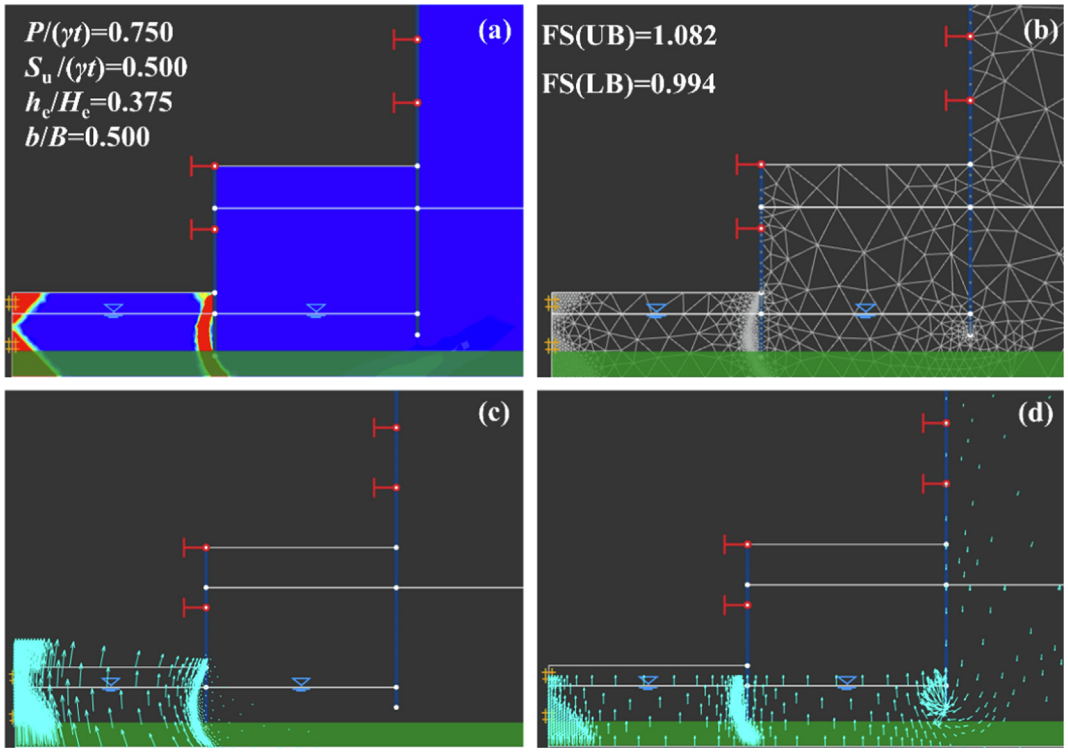

Fig. 9. Failure mode M5 of PIP braced excavation subjected to hydraulic uplift with $P/(\gamma t) = 0.750$, $S_u/(\gamma t) = 0.500$, $h_c/H_e = 0.375$ and $b/B = 0.500$: (a) shear dissipation contours, (b) adaptive meshes, (c) incremental displacement vectors, and (d) groundwater flow vectors.

move towards the centerline. Because the boundary condition of C. L. is assumed to be constrained horizontally, a plastic triangle zone with decreasing from bottom to top of the C. L. of PIP braced excavation is formed in Fig. 10, and the maximum horizontal compression strain is 54.78 %.

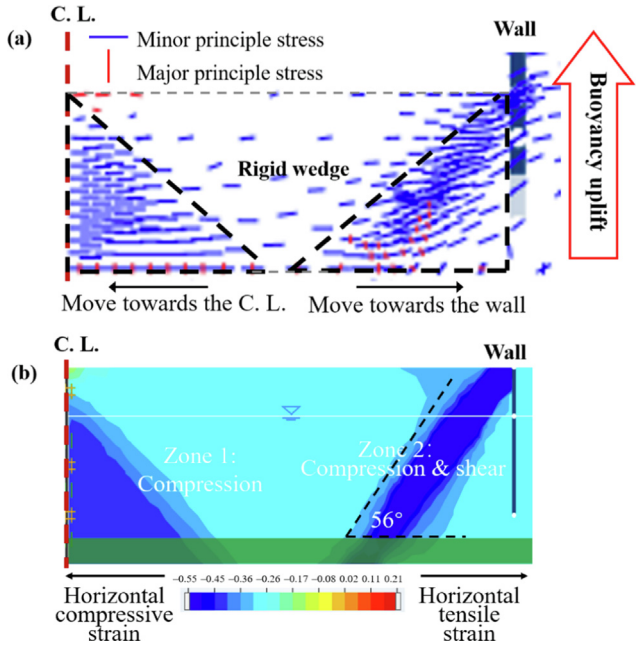

Fig. 10. Triggering mechanisms of combined failure mode: (a) computed principal stress distribution, and (b) computed horizontal strain.

The soils in Zone 2 move toward the diaphragm wall under the action of the shear force and horizontal compressive stress from the soil–wall interface; the linear slip surface is further formed, thus appearing the quasi-rigid wedge that is similar to that observed in the centrifugal tests by Sun (2016). Therefore, a PIP braced excavation above a confined aquifer bears not only buoyancy uplift, but also axial compression and shear force. In M3, the displacement vectors are mostly concentrated at the base of the inner pit under hydraulic uplift, and the transition zone is also accompanied by a certain amount of uplift deformations due to the unloading effect (see Fig. 7(c)). The soils behind the inner diaphragm wall tend to move into the pit, thus the entire circular surface occurs in the PIP braced excavation.

Hong et al. (2014) reported the triggering mechanism of the usual pit, that is, the clays inside the excavation fail in simple shear mode, while the ones outside the excavation remain stationary. In such a circumstance, only a vertical shearing band along with the soil–wall interface is observed. Directions of principal stresses in the failure zone are about 45° relative to the horizontal and vertical directions. The triggering mechanism due to basal hydraulic uplift for general excavations (without inner pit) is therefore complementally different from that in M3 for PIP excavations (Fig. 10). It is suggested that the design of a PIP braced excavation against failure modes M3 and M4 not only needs to improve the overall stability by increasing the stiffness of the supporting system, but also to increase the base stability of the inner pit against hydraulic uplift. Grouting or anti-uplift piles can be used to reinforce the base soils of the inner pit and transition zone. In addition, a reduction in upheaval deformations of the outer pit due to unloading of excavation would also be beneficial in enhancing the stability.

Figure 11 further explains the triggering mechanisms of basal hydraulic uplift in M5 for a relatively narrow inner pit. The slip surface near the diaphragm walls in the inner pit is not a vertical plane as assumed in the works by Yang and Zheng (2009), but an arc-shaped plane, indicating that rotational motion of soil mass near the wall occurred in the base of the inner pit. The base of the inner pit (so-called "clay beam") was divided into four zones (i.e., Zone 1, Zone 2, Zone 3, and Zone 4). As shown in Fig. 11, it can be found that the soils in Zone 1 mainly move toward the C. L. of the PIP system, and the maximum horizontal compressive strain is 22.20 %. The soils in Zone 2 move away from the C. L. under the action of tensile stress, and the maximum horizontal tensile strain is 10.75 %. Therefore, the soils inside the base of the inner pit near the C. L. appear a plastic zone similar to funnel shape.

Similarly, the soils located in front of soil–wall interfaces (Zone 3) are subjected to the compression and shear stress, and move towards the diaphragm wall, while the maximum compression strain is 26.02 %. The soils below the wall toe (Zone 4) subjected to tensile stress move away from the diaphragm wall, and the maximum tensile strain is 45.14 %. As a result, a neutral layer (i.e., horizontal displacement is zero near the centerline in x direction of clay beam) is formed under the comprehensive action of four zones, implying that the clay beam has also been subjected to bending, as shown in Fig. 11. Hence, in addition to the buoyancy uplift, PIP braced excavation in M3 is also subjected to axial tensile force, axial compressive force, and shear force.

It needs to be pointed out that the triggering mechanism due to the basal hydraulic uplift in M5 for PIP excavation

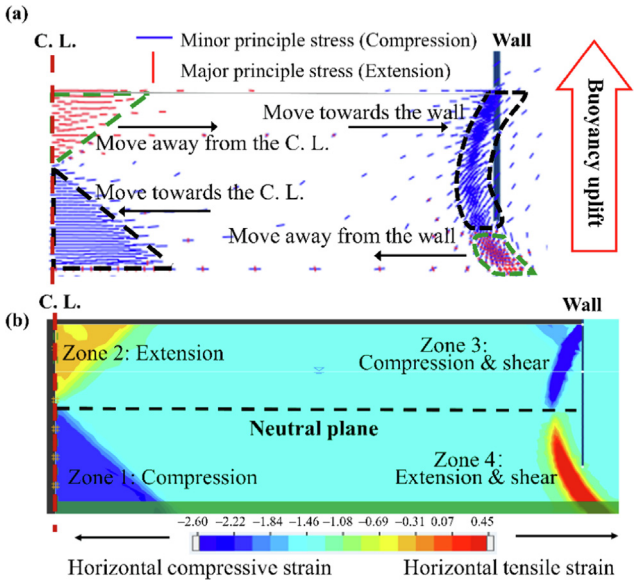

Fig. 11. Triggering mechanisms of failure mode of basal hydraulic uplift: (a) computed principal stress distribution, and (b) computed horizontal strain.

(Fig. 11) is similar to that for a usual foundation pit. Such a triggering mechanism is attributed to the soils inside the inner pit cannot resist the hydraulic uplift, despite the fact that the transition zone (similar to the soils outside the usual pit) is relatively stable.

5 Parametric studies

The FS against hydraulic uplift is an important parameter to evaluate the undrained stability of excavations. In the comparison section above, Fig. 4 shows that under the given normalized undrained shear strength of soils and geometric configuration of PIP braced excavation, FS value decreases nonlinearly with increasing the normalized artesian pressure. This section mainly examines the effects of normalized undrained shear strength ($S_u/(\gamma t)$) of AD, the ratio of inner pit width to outer pit width (b/B) and the ratio of inner pit depth to outer pit depth (h_e/H_e) on the FSs under the different normalized artesian pressure ($P/(\gamma t)$). It is worth noting that, for more clearly showing the change law of FS during parametric studies, a summary of FS and potential failure mode under various parametric combinations is also tabulated in Table 3.

5.1 Effect of undrained shear strength of AD

Figure 12 compares the variations in UB and LB solutions of FSs against hydraulic uplift with normalized undrained shear strength ($S_u/(\gamma t)$) of AD under different normalized artesian pressure ($P/(\gamma t)$). It can be seen that, for the studied range of normalized artesian pressure, the UB and LB solutions increase linearly with increasing $S_u/(\gamma t)$ value. At a given $S_u/(\gamma t)$, the UB and LB solutions decrease with increasing $P/(\gamma t)$ value. Furthermore, the FSs increase at a larger rate for the lower values of $P/(\gamma t)$. This is because when increasing the artesian pressure for a specific engineering case, the failure mode of the PIP excavation changes from one circular slip surface to basal hydraulic uplift, and the fewer soils can resist the artesian pressure. The results also show that the higher the normalized artesian pressure, the larger the normalized undrained shear strength of AD is required to keep stability.

5.2 Effect of ratio of inner pit width to outer pit width

Figure 13 plots the variations in the UB and LB solutions of FS against hydraulic uplift with the ratio of inner pit width to outer pit width (b/B) under different values of $P/(\gamma t)$. The plot indicates that, for b/B between 0.3 and 0.8, the UB and LB FSs decrease as the value of b/B increases nonlinearly for a given $P/(\gamma t)$. It is noted that the undrained stability of the PIP braced excavation subjected to hydraulic uplift gradually weakens. This indicates that the contributions of the platform between the inner and outer pits to the stability are reduced when increasing the inner pit width. Furthermore, the reduction law is more prominent for the larger $P/(\gamma t)$. At a given b/B, the FSs decrease at different rates with an increase in the value of $P/(\gamma t)$. The results also indicate that the higher the normalized artesian pressure, the lower ratio of inner pit width to outer pit width is required for the maintenance of stability.

5.3 Effect of ratio of inner pit depth to outer pit depth

Figure 14 gives the variations of UB and LB solutions of FS against hydraulic uplift with the ratio of inner pit depth to outer pit depth (h_e/H_e) under different normalized artesian pressures ($P/(\gamma t)$). Numerical results have shown that, at a given value of $P/(\gamma t)$, the UB and LB FSs decrease in a parabolic shape with increasing the value of h_e/H_e. This is because the reduction in the thickness of AD inside the inner pit causes the weaker ability of PIP braced excavation to resist hydraulic uplift. Note that, compared to Figs. 12 and 13, the variation ratio of FS is more obvious in Fig. 14, indicating that the ratio of inner pit depth to outer pit depth has the most significant influence on the stability of PIP braced excavations under the same value of $P/(\gamma t)$.

6 MARS-based empirical prediction

Section 5 examined the coupled effects of several dimensionless design parameters on the undrained stability of PIP excavations under the hydraulic uplift. It is highly difficult to present a closed-formed analytical solution to theoretically predict the FS under the coupled effects of re-excavation and hydraulic uplift, because of the underlying complexities and interactions involved. To achieve this, a MARS model is introduced here to present a new empirical prediction equation. The sensitivity is also explored with the MARS model.

6.1 Methodology of MARS

MARS is an outstanding regression model capable of efficiently capturing the nonlinear responses between input and output variables using a battery of piecewise linear functions (basic functions, BFs), as shown in Fig. 15. MARS can give greater flexibility because there is no specific need to predefine a functional relationship between the input and the output. The close approximation of MARS needs two steps called forward and backward iterative approaches. The first step required is to generate the potential BFs in the forward stepwise model. The expression of the global model including the linear combinations of potential BFs and interactions among them is shown in Eq. (8):

$$f(x) = \beta_0 + \sum_{m=1}^{M} \beta_m \lambda_m(X), \tag{8}$$

where β_0 is the constant, M is the number of BFs, λ_m is the m^{th} BF, and β_m is the coefficient of λ_m.

Note that the BF could be a spline function or the interaction of two or more spline functions, depending on the

Table 3
Artificial data set generated using FELA.

No.	$P/(\gamma t)$	$S_u/(\gamma t)$	b/B	h_e/H_e	FS	Mode	No.	$P/(\gamma t)$	$S_u/(\gamma t)$	b/B	h_e/H_e	FS	Mode
1	0.250	0.375	0.500	0.375	1.258	M2	41	0.500	0.750	0.600	0.375	1.555	M2
2	0.250	0.500	0.500	0.375	1.446	M2	42	0.500	0.750	0.700	0.375	1.494	M4
3	0.250	0.625	0.500	0.375	1.633	M2	43	0.500	0.750	0.800	0.375	1.402	M4
4	0.250	0.750	0.500	0.375	1.816	M1	44	0.625	0.750	0.300	0.375	1.570	M1
5	0.250	0.875	0.500	0.375	1.976	M1	45	0.625	0.750	0.400	0.375	1.535	M3
6	0.375	0.375	0.500	0.375	1.156	M2	46	0.625	0.750	0.500	0.375	1.478	M3
7	0.375	0.500	0.500	0.375	1.344	M2	47	0.625	0.750	0.600	0.375	1.409	M4
8	0.375	0.625	0.500	0.375	1.531	M2	48	0.625	0.750	0.700	0.375	1.330	M4
9	0.375	0.750	0.500	0.375	1.712	M2	49	0.625	0.750	0.800	0.375	1.223	M4
10	0.375	0.875	0.500	0.375	1.871	M2	50	0.750	0.750	0.300	0.375	1.441	M3
11	0.500	0.375	0.500	0.375	1.053	M3	51	0.750	0.750	0.400	0.375	1.371	M3
12	0.500	0.500	0.500	0.375	1.239	M3	52	0.750	0.750	0.500	0.375	1.279	M5
13	0.500	0.625	0.500	0.375	1.422	M3	53	0.750	0.750	0.600	0.375	1.180	M5
14	0.500	0.750	0.500	0.375	1.598	M3	54	0.750	0.750	0.700	0.375	1.055	M5
15	0.500	0.875	0.500	0.375	1.759	M3	55	0.750	0.750	0.800	0.375	0.925	M5
16	0.625	0.375	0.500	0.375	0.978	M3	56	0.250	0.750	0.500	0.125	3.058	M1
17	0.625	0.500	0.500	0.375	1.138	M3	57	0.250	0.750	0.500	0.187	2.503	M1
18	0.625	0.625	0.500	0.375	1.299	M3	58	0.250	0.750	0.500	0.252	2.095	M1
19	0.625	0.750	0.500	0.375	1.460	M3	59	0.250	0.750	0.500	0.313	1.875	M1
20	0.625	0.875	0.500	0.375	1.619	M3	60	0.250	0.750	0.500	0.375	1.816	M2
21	0.750	0.375	0.500	0.375	0.791	M5	61	0.375	0.750	0.500	0.125	2.935	M1
22	0.750	0.500	0.500	0.375	0.935	M5	62	0.375	0.750	0.500	0.187	2.389	M1
23	0.750	0.625	0.500	0.375	1.073	M5	63	0.375	0.750	0.500	0.252	1.997	M1
24	0.750	0.750	0.500	0.375	1.210	M5	64	0.375	0.750	0.500	0.313	1.775	M1
25	0.750	0.875	0.500	0.375	1.348	M5	65	0.375	0.750	0.500	0.375	1.712	M2
26	0.250	0.750	0.300	0.375	1.862	M1	66	0.500	0.750	0.500	0.125	2.845	M1
27	0.250	0.750	0.400	0.375	1.841	M1	67	0.500	0.750	0.500	0.187	2.275	M1
28	0.250	0.750	0.500	0.375	1.816	M2	68	0.500	0.750	0.500	0.252	1.891	M1
29	0.250	0.750	0.600	0.375	1.785	M2	69	0.500	0.750	0.500	0.313	1.675	M1
30	0.250	0.750	0.700	0.375	1.733	M2	70	0.500	0.750	0.500	0.375	1.598	M3
31	0.250	0.750	0.800	0.375	1.672	M4	71	0.625	0.750	0.500	0.125	2.731	M1
32	0.375	0.750	0.300	0.375	1.753	M1	72	0.625	0.750	0.500	0.187	2.175	M1
33	0.375	0.750	0.400	0.375	1.735	M1	73	0.625	0.750	0.500	0.252	1.761	M1
34	0.375	0.750	0.500	0.375	1.712	M2	74	0.625	0.750	0.500	0.313	1.565	M1
35	0.375	0.750	0.600	0.375	1.675	M2	75	0.625	0.750	0.500	0.375	1.500	M3
36	0.375	0.750	0.700	0.375	1.623	M4	76	0.750	0.750	0.500	0.125	2.625	M1
37	0.375	0.750	0.800	0.375	1.555	M4	77	0.750	0.750	0.500	0.187	2.075	M1
38	0.500	0.750	0.300	0.375	1.650	M1	78	0.750	0.750	0.500	0.252	1.647	M1
39	0.500	0.750	0.400	0.375	1.629	M1	79	0.750	0.750	0.500	0.313	1.475	M3
40	0.500	0.750	0.500	0.375	1.598	M2	80	0.750	0.750	0.500	0.375	1.418	M5

preferred settings. Subsequently, the generated BFs will be trained with the smallest errors, and then added into the MARS model one by one until reaching a predefined maximum of BFs. It follows that the MARS model may be overly fitted, and therefore, the second step is to delete the redundant BFs in the model using the backward pruning algorithm. In the following process, the BFs with the smallest contributions to the model will be deemed to be redundant and deleted using the GCV technique, which can be formulated as follows:

$$\mathrm{GCV} = \frac{\frac{1}{N}\sum_{i=1}^{N}[y_i - f(x_i)]^2}{\left[1 - \frac{M + d(M-1)/2}{N}\right]^2}, \tag{9}$$

where M and N are the numbers of BFs and data points, respectively; d is the penalty factor, and $f(x_i)$ is the predicted value from the MARS model. The term of $(M-1)/2$ is the number of knots. Therefore, the GCV value is penalized by the M and N to reduce the probability of overfitting. A default value of $d = 3$ is set in the MARS model (Friedman, 1991). In the backward pruning step, each BF is removed to minimize Eq. (9) until an optimal model with the smallest GCV value is suggested.

A variance decomposition procedure (ANOVA) involved in the MARS model was used to calculate the generalized cross-validation (GCV) value of each input variable, which enables further evaluation of the relative importance index (RII). At present, MARS has been widely used for the curve fitting in multi-dimensions for various geotechnical applications (Zhang et al., 2019, Zheng et al., 2020, Zhou et al., 2020a, Lai et al., 2021). More details can be found in Zhang (2020).

6.2 Sensitivity analyses

A generated artificial data set from the FELA model (see Table 3) was used for the sensitivity analyses of four dimensionless input variables (i.e., $S_u/(\gamma t)$, $P/(\gamma t)$, h_e/H_e,

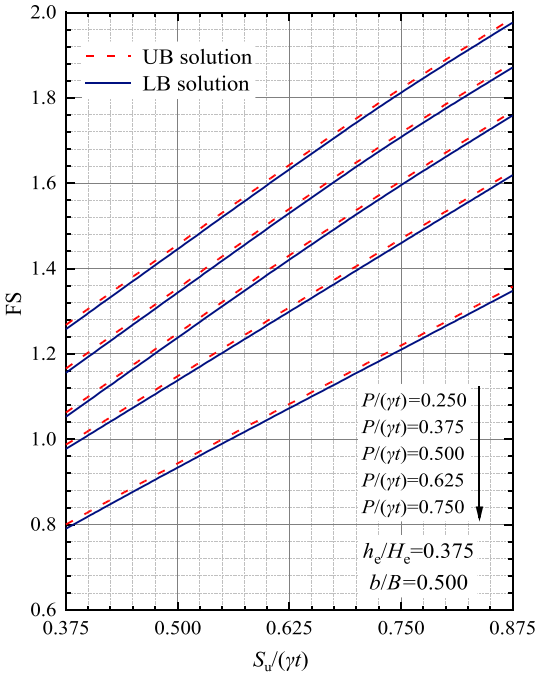

Fig. 12. Variations in UB and LB solutions of FSs with the normalized undrained shear strength of AD under different normalized artesian pressures.

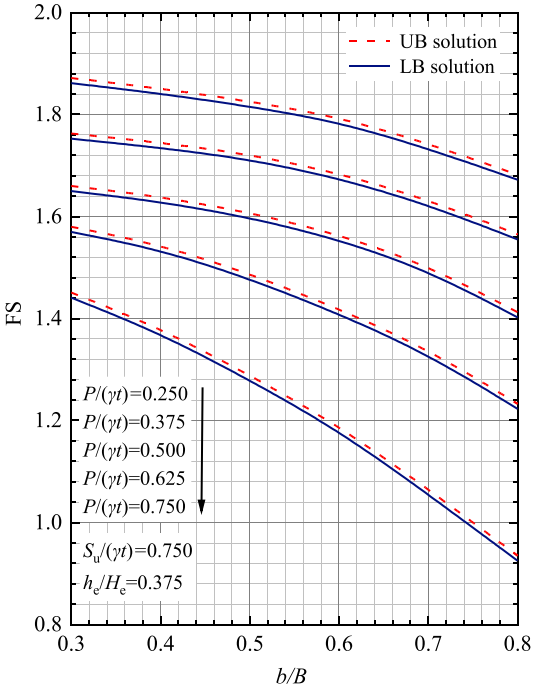

Fig. 13. Variations in UB and LB solutions of FSs with the ratio of inner pit width to outer pit width under different normalized artesian pressures.

and b/B) to the output variable, (i.e., the FSs against hydraulic uplift). Note that the LB solutions were chosen in the analyses as they could provide a safe estimate of the FS. The obtained RII of each input from the ANOVA

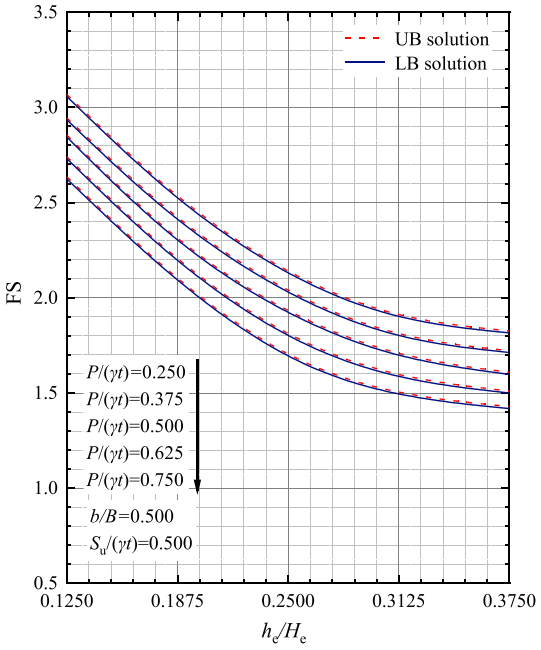

Fig. 14. Variations in UB and LB solutions of FSs with the ratio of inner pit depth to outer pit depth under different normalized artesian pressures.

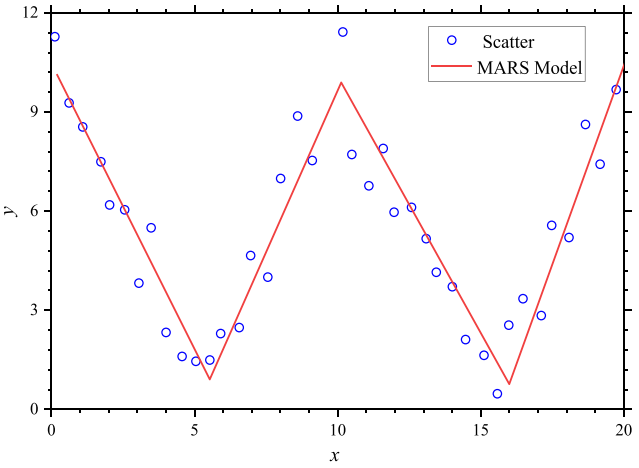

Fig. 15. Application of MARS model in a simple example (Adapted from Zhang (2020)).

procedure is presented in Fig. 16. RII value shows that the importance level (sensitivity) for FS, and RII of 100 % shows that the corresponding input variable has the most significant effect on *FS*. That is, the higher the RII value, the more sensitive the input variable. It can be found from Fig. 16 that h_e/H_e is the most influencing parameter on FS, followed by $P/(\gamma t)$, $S_u/(\gamma t)$ and b/B with RIIs of 46.14 %, 45.87 %, and 17.5 %, respectively. The study has shown that controlling the re-excavation depth of PIP excavations is the most effective countermeasure to resist hydraulic uplift failure. The effect of re-excavation width can be ignored for stability problems in design practices.

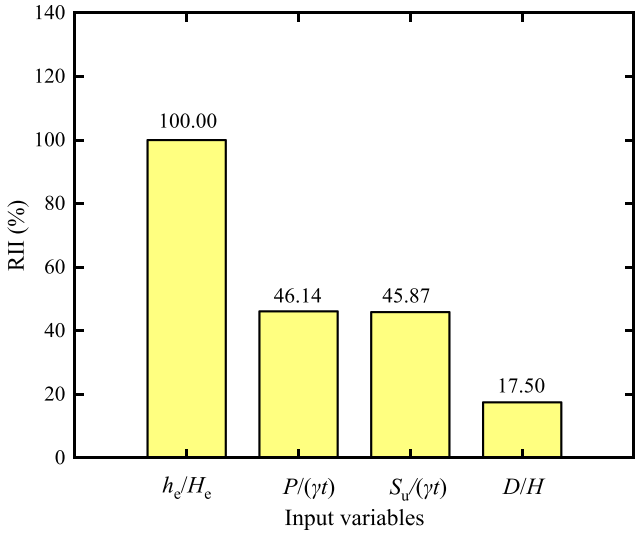

Fig. 16. RII of each input variable regarding FS.

6.3 New design equation

Eighty groups of LB solutions given in Table 3 were used to determine a design equation as functions of $S_u/(\gamma t)$, $P/(\gamma t)$, h_e/H_e, and b/B. Eight basic functions and the combined equation used for empirically predicting FS are shown in Table 4 and Eq. (10):

$$\begin{aligned} FS = {} & 2.121\text{–}0.628 \times BF1 + 7.695 \times BF2 - 0.782 \times BF3 \\ & + 11.155 \times BF4 - 1.530 \times BF5 - 4.646 \times BF6 \\ & - 0.365 \times BF7 - 1.089 \times BF8. \end{aligned} \tag{10}$$

To demonstrate the accuracy of the proposed design equation, a comparison between computed and predicted values is illustrated in Fig. 17. The coefficient of determination R^2 is very high at 99.4 %. The proposed design equation is sufficiently accurate to be used for predicting the FS.

In practice, $S_u/(\gamma t)$, $P/(\gamma t)$, h_e/H_e, and b/B can be used to determine each BF listed in Table 4 step by step. For a specific BF, it is needed to judge the maximum between zero and the calculated linear-functional value. In some cases, it is necessary to multiply the maximum by the other BFs. The calculated value of each BF can be substituted into Eq. (10) to yield the predicted result.

Table 4
Basis functions and mathematical equations in MARS model for FS.

BF	Equation
BF1	$\max(0, h_e/H_e - 0.252)$
BF2	$\max(0, 0.252 - h_e/H_e)$
BF3	$\max(0, P/(\gamma t) - 0.250)$
BF4	$\max(0, S_u/(\gamma t) - 0.375) \times$ BF1
BF5	$\max(0, b/B - 0.600) \times$ BF3
BF6	$\max(0, P/(\gamma t) - 0.625) \times$ BF1
BF7	$\max(0, b/B - 0.300)$
BF8	$\max(0, P/(\gamma t) - 0.500) \times$ BF7

$FS = 2.121\text{–}0.628 \times BF1 + 7.695 \times BF2 - 0.782 \times BF3$

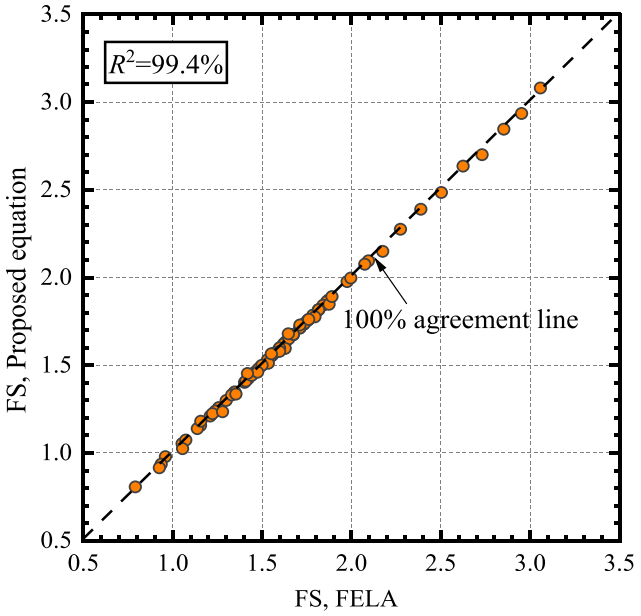

Fig. 17. Comparison of the FSs between the proposed equation and FELA.

7 Conclusions

This study analyzed the undrained stability of PIP excavations subjected to hydraulic uplift using the FELA method. A hypothetical numerical model was first presented to account for the coupling effects of re-excavation and hydraulic uplift. To validate the accuracy of FELA, a brief comparison to existing design methods was carried out. A large number of FELAs were then performed on PIP braced excavations in the soft clays overlying a confined aquifer. The numerical results showed that different triggering and failure mechanisms could be formed in the PIP system, mainly depending on the combination of normalized artesian pressure ($P/(\gamma t)$), undrained shear strength of AD ($S_u/(\gamma t)$), the ratio of inner pit width to outer pit width (h_e/H_e), and the ratio of inner pit depth to outer pit depth (b/B). Parametric studies were subsequently carried out to study the effects of four dimensionless parameters (i.e. $S_u/(\gamma t)$, $P/(\gamma t)$, h_e/H_e, and b/B) on FS of PIP system. The MARS model, capable of accurately capturing the nonlinear relationships between a set of input variables and output variables, was used to assess the sensitivity of the studied parameters. The generated artificial data from FELA were used for the sensitivity analyses and empirical curve fitting.

The main conclusions can be drawn as follows:

(1) There are three typical failure modes of PIP braced excavation subjected to hydraulic uplift: circular failure surface for the outer pit, basal hydraulic uplift, and combined failure, regardless of the difference in slip surface shapes. For the basal hydraulic uplift, the basal soils of the inner pit are mainly subjected

to axial compression, axial tension, shear stress, and buoyancy. This may correspond to uplift, rotation, and bending mechanisms; consequently, a neutral layer in the base of the inner pit is formed. For the combined failure mode, the basal soils inside the inner pit are mainly subjected to horizontal compressive stress, shear stress, and buoyancy uplift; the quasi-rigid wedge inside the inner pit might be formed.

(2) The UB and LB solutions of FS increase linearly with increasing the value of $S_u/(\gamma t)$, but decrease nonlinearly as the values of h_e/H_e and b/B increase. All these variation laws are predominant when the values of $P/(\gamma t)$ is large, with the basal hydraulic uplift occurring in the inner pit. Moreover, compared with the other sensitive factors under the same artesian pressure, h_e/H_e has the most significant effects on the stability of PIP braced excavations.

(3) Although the variation laws of UB and LB solutions of FS determined by the FELA method might be similar to those of existing design methods which simplify the PIP excavation as single excavation, the existing design methods for assessing the undrained stability of a PIP braced excavation cannot consider the coupling effect of re-excavation and hydraulic uplift. The obtained theoretical solutions from them are lower than those provided by UB and LB solutions by FELA. A new design equation based on the MARS model is thus presented to predict FS under various cases.

It should to be noted that, although the base case is a hypothetical and simplified numerical model, the conclusions and interpretation of triggering and failure mechanisms subjected to hydraulic uplift were drawn from a wide range of practical cases. However, they may be limited for complex ground strata with multi-aquifer-aquitard systems, in particular for empirical prediction of FSs with the MARS model presented in this study. This would be the focus of a follow-up work in the future.

Declaration of Competing Interest

The authors declare that they have no known competing financial interests or personal relationships that could have appeared to influence the work reported in this paper.

Acknowledgments

This study is financially supported by the National Natural Science Foundation of China (Grant No. 41972269), Fundamental Research Funds for the Central Universities of China (Grant No. 2242022 k30055), Postgraduate Research & Practice Innovation Program of Jiangsu Province (Grant No. KYCX20_0118), Scientific Research Foundation of Graduate School of Southeast University (Grant No. YBPY2041) and CSC Scholarships.

References

Bolton, M. (1986). The strength and dilatancy of sands. *Géotechnique, 36*(1), 65–78.
Brinkgreve, R., Broere, W., & Waterman, D. (2002). Plaxis 2D-version 8. Swets and Zeitlinger Publishers.
Cashman, P. M., & Preene, M. (2003). Groundwater Lowering in Construction. Boca Raton: CRC Press.
Chen, F., Miao, G., & Lai, F. (2020). Base instability triggered by hydraulic uplift of pit-in-pit braced excavations in soft clay overlying a confined aquifer. *KSCE Journal of Civil Engineering, 24*(6), 1717–1730.
Chen, W. (1975). Limit Analysis and Soil Plasticity. New York: Elsevier Scientific Pub. Co.
Chow, H. L., & Ou, C. Y. (1999). Boiling failure and resumption of deep excavation. *Journal of Performance of Constructed Facilities, 13*(3), 114–120.
Ding, C., Li, Z., Wu, X., & Wu, K. (2014). Analysis on inducing factors to inrushing plastic deformation failure of foundation pit with confined water. In *Tunneling and Underground Construction, Shanghai, China* (pp. 491–501).
Doherty, J. P., & Muir Wood, D. (2013). An extended Mohr-Coulomb (EMC) model for predicting the settlement of shallow foundations on sand. *Géotechnique, 63*, 661–673.
Friedman, J. H. (1991). Multivariate adaptive regression splines. *The Annals of Statistics, 19*(1), 1–67.
Hong, Y., & Ng, C. W. W. (2013). Base stability of multi-propped excavations in soft clay subjected to hydraulic uplift. *Canadian Geotechnical Journal, 50*(2), 153–164.
Hong, Y., Ng, C. W. W., & Wang, L. Z. (2014). Initiation and failure mechanism of base instability of excavations in clay triggered by hydraulic uplift. *Canadian Geotechnical Journal, 52*(5), 599–608.
Hong, Y., Ng, C. W. W., & Wang, L. Z. (2015). Initiation and failure mechanism of base instability of excavations in clay triggered by hydraulic uplift. *Canadian Geotechnical Journal, 52*(5), 1–10.
Hong, Y., & Wang, L. (2016). Deformation and Failure Mechanism of Excavation in Clay Subjected to Hydraulic Uplift. Hangzhou, China: Springer.
Ke, L., Gao, Y., Li, D., Zhang, J., & Ji, J. (2020). Undrained stability analysis of trenches for buried submarine pipelines. *Marine Georesources and Geotechnology, 38*(5), 583–594.
Keawsawasvong, S., & Ukritchon, B. (2017a). Stability of unsupported conical excavations in non-homogeneous clays. *Computers and Geotechnics, 81*, 125–136.
Keawsawasvong, S., & Ukritchon, B. (2017b). Undrained limiting pressure behind soil gaps in contiguous pile walls. *Computers and Geotechnics, 83*, 152–158.
Keawsawasvong, S., & Ukritchon, B. (2017c). Undrained stability of an active planar trapdoor in non-homogeneous clays with a linear increase of strength with depth. *Computers and Geotechnics, 81*, 284–293.
Keawsawasvong, S., & Ukritchon, B. (2019). Undrained basal stability of braced circular excavations in non-homogeneous clays with linear increase of strength with depth. *Computers and Geotechnics, 115*, 103180.
Krabbenhoft, K., Lyamin, A., Krabbenhoft, J., 2015. Optum computational engineering (OptumG2). Computer Software. https://www.optumce.com.
Lai, F., Chen, S., Xue, J., & Chen, F. (2020a). New analytical solutions for shallow cohesive soils overlying trench voids under various slip surfaces. *Transportation Geotechnics, 25*, 100411.
Lai, F., Liu, S., Deng, Y., Sun, Y., Wu, K., & Liu, H. (2020b). Numerical investigations of the installation process of giant deep-buried circular open caissons in undrained clay. *Computers and Geotechnics, 118*, 103322.
Lai, F., Liu, S., Li, Y., & Sun, Y. (2022a). A new installation technology of large diameter deeply-buried caissons: Practical application and observed performance. *Tunnelling and Underground Space Technology, 125*, 104507.
Lai, F., Yang, D., Liu, S., Zhang, H., & Cheng, Y. (2022b). Towards an improved analytical framework to estimate active earth pressure in narrow c–ϕ soils behind rotating walls about the base. *Computers and Geotechnics, 141*, 104544.
Lai, F., Zhang, N., Liu, S., Sun, Y., & Li, Y. (2021). Ground movements induced by installation of twin large diameter deeply-buried caissons: 3D numerical modeling. *Acta Geotechnica, 16*(9), 2933–2961.

Liu, G. B., Jiang, R. J., Ng, C. W., & Hong, Y. (2011). Deformation characteristics of a 38 m deep excavation in soft clay. *Canadian Geotechnical Journal, 48*(12), 1817–1828.
Milligan, V., & Lo, K. (1970). Observations on some basal failures in sheeted excavations. *Canadian Geotechnical Journal, 7*(2), 136–144.
Moore, J., & Longworth, T. (1979). Hydraulic uplift of the base of a deep excavation in Oxford Clay. *Géotechnique, 29*(1), 35–46.
Ng, C. W. W., Hong, Y., Liu, G. B., & Liu, T. (2012). Ground deformations and soil-structure interaction of a multi-propped excavation in Shanghai soft clays. *Géotechnique, 62*(10), 907–921.
Oberhollenzer, S., Tschuchnigg, F., & Schweiger, H. F. (2018). Finite element analyses of slope stability problems using non-associated plasticity. *Journal of Rock Mechanics and Geotechnical Engineering, 10*(6), 1091–1101.
Peng, C.-X., Liu, N.-W., Li, M.-G., Zhen, L., & Chen, J.-J. (2022). Hydro-mechanical coupled analyses on wall deformations caused by deep excavations and dewatering in a confined aquifer. *Acta Geotechnica, 17*, 2465–2479.
Pujades, E., Vàzquez-Suñé, E., Carrera, J., & Jurado, A. (2014). Dewatering of a deep excavation undertaken in a layered soil. *Engineering Geology, 178*(15), 15–27.
Shi, Y.-J., Li, M.-G., Zhang, Y.-Q., Li, J., & Wang, J.-H. (2018). Field investigation and prediction of responses of far-field ground and groundwater to pumping artesian water in deep excavations. *International Journal of Geomechanics, 18*(10), 04018132.
Shiau, J., Keawsawasvong, S., & Lee, J.-S. (2022). Three-dimensional stability investigation of trapdoors in collapse and blowout conditions. *International Journal of Geomechanics, 22*(4), 04022007.
Shiau, J., Lee, J.-S., & Al-Asadi, F. (2021). Three-dimensional stability analysis of active and passive trapdoors. *Tunnelling and Underground Space Technology, 107*, 103635.
Sloan, S. (2013). Geotechnical stability analysis. *Géotechnique, 63*(7), 531–571.
Sloan, S. W., & Kleeman, P. W. (1995). Upper bound limit analysis using discontinuous velocity fields. *Computer Methods in Applied Mechanics & Engineering, 127*(1), 293–314.
Sun, Y.-Y. (2016). Experimental and theoretical investigation on the stability of deep excavations against confined aquifers in Shanghai, China. *KSCE Journal of Civil Engineering, 20*(7), 2746–2754.
Sun, Y., & Xiao, H. (2021). Wall Displacement and Ground-Surface Settlement Caused by Pit-in-Pit Foundation Pit in Soft Clays. *KSCE Journal of Civil Engineering, 25*(4), 1262–1275.
Sun, Y., Zhao, Y., & Zhang, D. (2018). Surface subsidence of pit-in-pit foundation in sand–cobble stratum in Beijing area. *Proceedings of the Institution of Civil Engineers–Ground Improvement, 172*(2), 96–107.
Sun, Y., Zhou, S., & Luo, Z. (2017). Basal-heave analysis of pit-in-pit braced excavations in soft clays. *Computers and Geotechnics, 81*, 294–306.
Tan, Y., Lu, Y., Xu, C., & Wang, D. (2018). Investigation on performance of a large circular pit-in-pit excavation in clay-gravel-cobble mixed strata. *Tunnelling and Underground Space Technology, 79*, 356–374.
Terzaghi, K. (1943). Theoretical Soil Mechanics. New York: John Wiley and Sons.
Terzaghi, K., Peck, R. B., & Mesri, G. (1968). Soil Mechanics in Engineering Practice. John Wiley & Sons.
Tiwari, B., Ye, G., Li, M., Khalid, U., & Yadav, S. K. (2020). Strength and dilatancy behaviors of deep sands in Shanghai with a focus on grain size and shape effect. *Journal of Rock Mechanics and Geotechnical Engineering, 12*(6), 1214–1225.
Tschuchnigg, F., Schweiger, H., & Sloan, S. W. (2015). Slope stability analysis by means of finite element limit analysis and finite element strength reduction techniques. Part I: Numerical studies considering non-associated plasticity. *Computers and Geotechnics, 70*, 169–177.
Wang, Y., Li, B., Chen, C., & Jia, H. (2020). Influence of groundwater level fluctuation on lateral deformation of cantilever enclosure structure of pit-in-pit. *Marine Georesources and Geotechnology, 38*(1), 108–113.
Wood, D. M. (2004). Geotechnical modelling. US: CRC Press.
Wu, C.-J., Ye, G.-L., Zhang, L.-L., Bishop, D., & Wang, J.-H. (2015). Depositional environment and geotechnical properties of Shanghai clay: A comparison with Ariake and Bangkok clays. *Bulletin of Engineering Geology and the Environment, 74*(3), 717–732.
Wu, Y. X., Shen, S. L., & Yuan, D. J. (2016). Characteristics of dewatering induced drawdown curve under blocking effect of retaining wall in aquifer. *Journal of Hydrology, 539*, 554–566.
Wudtke, R.-B. (2008). Failure mechanisms of hydraulic heave at excavations. *19th European young geotechnical engineers' conference. Gyor, Hungary*.
Wudtke, R.-B., & Witt, K. J. (2006). A static analysis of hydraulic heave in cohesive soil. In *Proceedings 3rd International Conference on Scour and Erosion (ICSE-3)*. November 1–3, 2006, Amsterdam, The Netherlands (pp. 721–726).
Yang, D., Lai, F., & Liu, S. (2022). Earth pressure in narrow cohesive-fictional soils behind retaining walls rotated about the top: An analytical approach. *Computers and Geotechnics, 149*, 104849.
Yang, J., & Zheng, G. (2009). Classification of seepage failures and opinion to formula for check bursting instability in dewatering. *Rock Soil Mech., 30*(1), 261–264 (in Chinese).
Yang, S., Leshchinsky, B., Zhang, F., & Gao, Y. (2016). Required strength of geosynthetic in reinforced soil structures supporting spread footings in three dimensions. *Computers and Geotechnics, 78*, 72–87.
Ye, G.-L., Lin, N., Bao, X.-H., Gu, L., & Yadav, S. K. (2018). Effect of Quaternary transgression and regression on the engineering properties of Shanghai soft clays. *Engineering Geology, 239*, 321–329.
Ye, G.-L., & Ye, B. (2016). Investigation of the overconsolidation and structural behavior of Shanghai clays by element testing and constitutive modeling. *Underground Space, 1*(1), 62–77.
Zhang, L., Ying, H., Xie, K., & Huang, D. (2016). Effect of Groundwater Fluctuations on Pore Pressures and Earth Pressures on Coastal Excavation Retaining Walls. *Marine Georesources and Geotechnology, 34*(8), 770–781.
Zhang, W. (2020). *MARS Applications in Geotechnical Engineering Systems*. Springer.
Zhang, W., Zhang, R., Wang, W., Zhang, F., & Goh, A. T. C. (2019). A Multivariate Adaptive Regression Splines model for determining horizontal wall deflection envelope for braced excavations in clays. *Tunnelling and Underground Space Technology, 84*, 461–471.
Zhang, Y.-Q., Wang, J.-H., & Li, M.-G. (2018). Effect of dewatering in a confined aquifer on ground settlement in deep excavations. *International Journal of Geomechanics, 18*(10), 04018120.
Zheng, G., He, X., Zhou, H., Yang, X., Yu, X., & Zhao, J. (2020). Prediction of the tunnel displacement induced by laterally adjacent excavations using multivariate adaptive regression splines. *Acta Geotechnica, 15*(8), 2227–2237.
Zhou, H.-Z., Zheng, G., He, X.-P., Wang, E.-Y., Guo, Z.-Y., Nie, D.-Q., & Ma, S.-K. (2020a). Numerical modelling of retaining structure displacements in multi-bench retained excavations. *Acta Geotechnica, 15*(9), 2691–2703.
Zhou, H., Liu, H., Li, Y., & Ding, X. (2020b). Limit lateral resistance of XCC pile group in undrained soil. *Acta Geotechnica, 15*(6), 1673–1683.
Zhou, N., Vermeer, P. A., Lou, R., Tang, Y., & Jiang, S. (2010). Numerical simulation of deep foundation pit dewatering and optimization of controlling land subsidence. *Engineering Geology, 114*(3), 251–260.